

Article

Design and Analysis of Compact High-Performance Lithium–Niobate Electro–Optic Modulator Based on a Racetrack Resonator

Zixin Chen ^{1,2,3}, Jianping Li ^{1,2,3,*}, Weiqin Zheng ^{1,2,3}, Hongkang Liu ^{1,2,3}, Quandong Huang ^{1,2,3}, Ya Han ^{1,2,3} and Yuwen Qin ^{1,2,3} 

¹ Institute of Advanced Photonics Technology, School of Information Engineering, Guangdong University of Technology, Guangzhou 510006, China

² Key Laboratory of Photonic Technology for Integrated Sensing and Communication, Ministry of Education, Guangdong University of Technology, Guangzhou 510006, China

³ Guangdong Provincial Key Laboratory of Information Photonics Technology, Guangdong University of Technology, Guangzhou 510006, China

* Correspondence: jianping@gdut.edu.cn

Abstract: With the ever-growing demand for high-speed optical communications, microwave photonics, and quantum key distribution systems, compact electro-optic (EO) modulators with high extinction ratios, large bandwidth, and high tuning efficiency are urgently pursued. However, most integrated lithium–niobate (LN) modulators cannot achieve these high performances simultaneously. In this paper, we propose an improved theoretical model of a chip-scale electro-optic (EO) microring modulator (EO-MRM) based on X-cut lithium–niobate-on-insulator (LNOI) with a hybrid architecture consisting of a 180-degree Euler bend in the coupling region, double-layer metal electrode structure, and ground–signal–signal–ground (G-S-S-G) electrode configuration, which can realize highly comprehensive performance and a compact footprint. After parameter optimization, the designed EO-MRM exhibited an extinction ratio of 38 dB. Compared to the structure without Euler bends, the increase was 35 dB. It also had a modulation bandwidth of 29 GHz and a tunability of 8.24 pm/V when the straight waveguide length was 100 μm . At the same time, the proposed device footprint was $1.92 \times 10^4 \mu\text{m}^2$. The proposed MRM model provides an efficient solution to high-speed optical communication systems and microwave photonics, which is helpful for the fabrication of high-performance and multifunctional photonic integrated devices.

Keywords: TFLN; MRM; EOM; high extinction ratio; small footprint



Received: 19 December 2024

Revised: 12 January 2025

Accepted: 15 January 2025

Published: 17 January 2025

Citation: Chen, Z.; Li, J.; Zheng, W.; Liu, H.; Huang, Q.; Han, Y.; Qin, Y.

Design and Analysis of Compact High-Performance Lithium–Niobate Electro–Optic Modulator Based on a Racetrack Resonator. *Photonics* **2025**, *12*, 85. <https://doi.org/10.3390/photonics12010085>

Copyright: © 2025 by the authors. Licensee MDPI, Basel, Switzerland. This article is an open access article distributed under the terms and conditions of the Creative Commons Attribution (CC BY) license (<https://creativecommons.org/licenses/by/4.0/>).

1. Introduction

Lithium–niobate (LN) has been widely used in various photonic devices due to its broad transparent operational window, strong electro-optic (EO) effect, large nonlinear coefficient, and chemical stability [1,2]. In recent years, the LN-on-insulator (LNOI) has become highly attractive due to its ease of fabrication and sub-micron-scale waveguide structures [3–5]. Specifically, the various EO modulators (EOMs) based on the LNOI platform have become the focus of research [6,7]. These EOMs, including phase modulators (PMs) [8], Mach–Zehnder modulators (MZMs) [9,10], microring modulators (MRMs) [11,12], and photonic crystal resonator modulators (PHCMs) [13], are key components and required in various optical communication systems to realize the conversion of electrical signals to optical signals [14,15].

Currently, the EO-MRM with a resonant structure has been widely researched due to the ability of device size reduction [16–22]. More attractively, extensive studies on thin-film LN (TFLN)-based EO-MRMs have been implemented theoretically and experimentally [11,12,23–27]. For example, C. Wang et al. demonstrated a monolithically integrated EO-MRM by shaping TFLN into sub-wavelength structures with a tuning efficiency of 7 pm/V and Q factor of 50,000 [11]. R. Ahmed et al. reported a Si_3N_4 -X-cut LiNbO_3 -based modified racetrack resonator which performs at both DC and heightened frequencies [23]. This modulator features a measured tunability and intrinsic quality factor (Q) of 2.9 pm/V and 1.3×10^5 , respectively. However, the high Q property of these modulators limits their modulation bandwidth to below a few gigahertz [28]. In addition, M. Bahadori et al. designed a highly compact Z-cut TFLN EO-MRM with a symmetric electrode configuration, which exhibited a high extinction ratio (ER, 20 dB) and large modulation bandwidth (BW, over 28 GHz) and EO tuning efficiency (9 pm/V), [24]. However, Z-cut LN films only work for TM polarization and are not suitable for on-chip integration [29]. Hence, considering the development of a chip-scale photonic circuit and the need for high performance, the X-cut TFLN EO-MRM remains to be further researched so as to make full use of the advantages of LN.

In this work, aiming to improve the performance of the X-cut TFLN EO-MRM, a novel MRM theoretical model was proposed and numerically analyzed. In this model, a 180-degree Euler bend was designed in the coupling region to enhance the modulation bandwidth, which is limited by the photon lifetime, and reduce the device footprint. At the same time, a G-S-S-G power-on mode and double-layer metal electrode were adopted to increase the fraction of the microring exposed to the EO effect and the variation in the refractive index after power-on, thereby improving the tuning efficiency. The final simulation results show that the proposed EO-MRM model could realize an ER of up to 38 dB and a BW of 29 GHz along with a tunability of up to 8.24 pm/V. In a comparison with the reported works, our model outperforms the corresponding MRM performances and has potential in high-speed optical communications.

2. Structure Design

The structure of our proposed EO-MRM is shown in Figure 1a. A modified racetrack microring with a 180-degree Euler bend in the coupling region was designed, which aims to reduce the transmission coefficient t and increase the coupling coefficient κ , thereby expanding the bandwidth of the device and enhancing the extinction ratio. Additionally, the double-layer metal electrodes were loaded on both sides of the straight waveguides with a G-S-S-G electrode design. The dominant component of the quasi-TE mode E_x is in the same direction as the applied electric field and the direction of the maximum electric–optic coefficient of the X-cut TFLN, leading to strong optical confinement and efficient electro-optic modulation. In this model, we chose a 600 nm-thick LN film which is commercially available and can be processed for semi-etching with a sidewall angle (θ) of 72° , matching well with the state of the art of LN ridge waveguides [2–5]. Moreover, the thickness of the upper metal electrode was set at 400 nm to take into account that the lift-off process is easier to achieve during the preparation process, and it can improve the coupling between the optical mode and the modulation field as well as the optical propagation loss. In order to achieve the desired extinction ratio, bandwidth, and tuning efficiency, parameters such as the coupling coefficient κ and the transmission coefficient t in the coupling region, the attenuation factor α in the microring, metal loss, and the filling factor ff (representing the fraction of the microring exposed to EO perturbation) need to be finely optimized. It should be noted that these changes must be made in a manner that allows the proposed design to be optimized and manufactured. Accordingly, we

used numerical methods based on the finite-difference time-domain (FDTD) method and a combination of MATLAB and the finite-element method (FEM) to simulate the performance of our proposed EO-MRM structure.

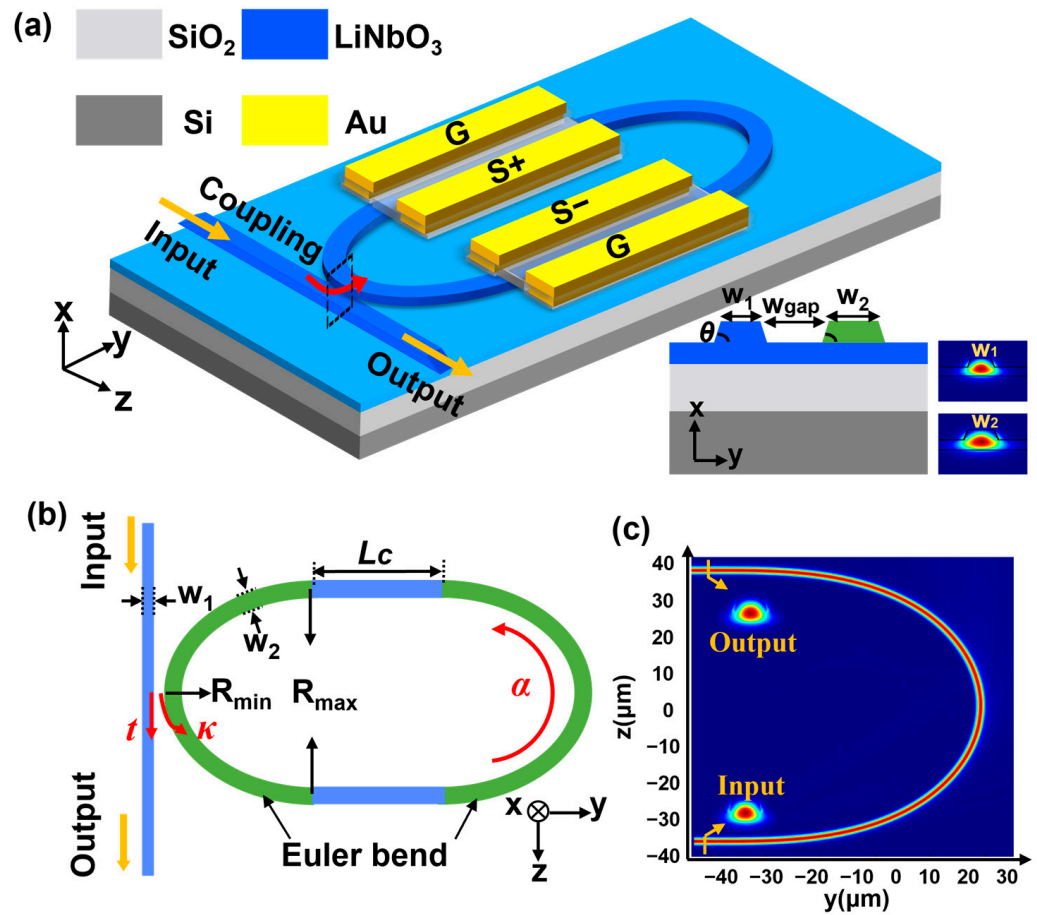


Figure 1. (a) A schematic diagram of the proposed racetrack resonator with a double-layer electrode. Inset: the cross-section of coupling area. (b) A top view of the racetrack microring resonator. (c) The optical mode field and intensity distribution of the Euler bend with a waveguide width of $0.8 \mu\text{m}$, simulated by FDTD.

Figure 2a,b present the calculated outcomes of the mode field and effective refractive index obtained by the finite-difference eigenmode (FDE) solver. At a wavelength of 1550 nm , the effective refractive index is approximately 1.884 . Given the selected parameters, the microring resonator is capable of transmitting the TE_0 mode in the vicinity of 1550 nm with relatively low loss, thereby accomplishing effective optical mode confinement as well as propagation. Through numerical simulation, the figure of merit (FOM) of the waveguide was calculated as being $\sim 1.234 \times 10^4$ using the method in the reference [30].

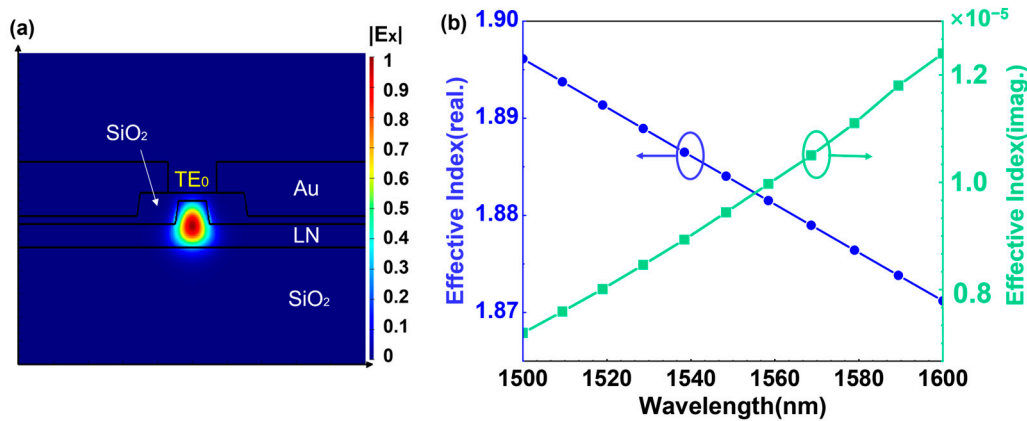


Figure 2. (a) Lumerical MODE simulation of the fundamental TE₀ optical mode of the waveguide. (b) The calculated optical effective index of the waveguide.

3. Theoretical MRM Model Analysis

3.1. Microring Resonator Optimization

We carried out simulations of the transmission spectra of the microring resonator by using the transfer matrix method. During this process, the conditions for resonance generation $\theta = 2\pi m$ (θ is the phase difference; m is the resonant order) in the microring as well as the phase difference $\theta = \beta L$ (β is the propagation constant) caused by the light propagating around the microring for one cycle were taken into consideration. In this designed structure, the performance of the coupling region is one of the most important parts of realizing the high ER and large BW, which has a significant influence on the EO-MRM. As shown in Figure 1b, the microring structure consists of curved waveguides and the input waveguide. The ER is defined as the ratio between the maximum and minimum power at the output end to quantify the depth of resonance peaks and can be expressed as follows:

$$ER = \frac{T_{max}}{T_{min}} = 10 \lg \left[\frac{(t + \alpha)(1 - \alpha t)}{(t - \alpha)(1 + \alpha t)} \right]^2 \tag{1}$$

where α is the attenuation factor for one round of light transmission in the microring, which is dimensionless, and α equals 1 for zero loss. The parameter t is the amplitude transmission coefficient in the coupling region, also known as the self-coupling coefficient, while κ is the amplitude coupling coefficient in the coupling region, also known as the cross-coupling coefficient. Assuming that the coupling region is lossless, then $|\kappa|^2 + |t|^2 = 1$. Moreover, the transmittance T is positively correlated with the coupling coefficient κ . To enhance the ER of the microring resonator, it is necessary to appropriately increase the coupling coefficient κ while maintaining a certain operating state of the microring. Equation (1) shows that the relative magnitudes of t and α determine the operating state of the microring resonator. When $t = \alpha$, the microring is in the critical coupling state and reaches the optimal resonant state with the maximum transmission power. Thus, to improve the ER of the microring modulator, it is preferred that the microring operates near the critical coupling state. By calculation, when the coupling coefficient κ^2 is approximately 0.15, the proposed modulator operates in the critical coupling state and a high ER can be achieved.

The quality factor (Q) measures the ability of a resonant cavity to store energy and can be characterized using the linewidth method and defined as the ratio of the peak wavelength to the full width at the half-maximum (FWHM). For an all-pass microring resonator, its Q value can be expressed as follows:

$$Q = \frac{\omega}{\Delta\omega_{FWHM}} \approx \frac{\lambda_0}{\Delta\lambda_{FWHM}} = \frac{\pi \cdot n_{eff} \cdot L}{\lambda_0} \frac{\sqrt{\alpha t}}{1 - \alpha t} \tag{2}$$

where λ_0 is the peak wavelength and L is the cavity length of the resonator.

Modulation bandwidth is an important performance parameter of electro-optic modulators. For EO-MRMs, it is usually determined jointly by the optical response and the electrical response of the device [31]. Compared to the influence of the optical bandwidth on its modulation bandwidth, the impact of the electrical bandwidth on the TFLN EO-MRM is relatively small. The main factor limiting the bandwidth is the time required to build up the optical field within the ring resonator. Then, the modulation bandwidth of a ring resonator is given by

$$BW = \frac{c}{\lambda_0 \cdot Q} = \frac{\Delta\omega_{FWHM}}{2\pi} \quad (3)$$

Thus, the bandwidth of a microring modulator is constrained by its Q factor, namely the linewidth FWHM. Considering the limitation of photon lifetime on the modulation speed, the Q factor should be carefully weighed in the design stage to achieve a larger modulation bandwidth [6]. As indicated by Equation (2), the Q factor is influenced by the attenuation factor α and the transmission coefficient t . The attenuation factor α satisfies the relationship, with the radius of the microring r and the transmission loss a (cm^{-1}). The transmission loss a is inversely related to the attenuation factor α , implying that a larger transmission loss results in a smaller attenuation factor. However, when designing the microring resonator, it is generally preferred to minimize the transmission loss because increasing the transmission loss will lead to adverse effects such as reduced signal-to-noise ratio and enhanced nonlinear effects in the modulator [32]. Therefore, to restrict the Q factor, a strategy of reducing the transmission coefficient t was adopted. If the target bandwidth is set to be 30 GHz, the Q factor is calculated to be approximately 6500 according to Equation (3). According to the analysis above, the 180-degree Euler bends were utilized in the coupling region of the microring resonator, aiming to increase the coupling coefficient κ , reduce the transmission coefficient t , and thereby achieve a high ER and large BW for the MRM.

Euler bends were drawn in MATLAB with a waveguide width of $0.8 \mu\text{m}$, a radius R_{\min} of $30 \mu\text{m}$, and a radius R_{\max} of $1500 \mu\text{m}$ based on the microwave waveguide structure with modified Euler curves [33,34]. This set of parameters was selected because it shows a relatively low loss in the quasi-TE mode transmission within the C-band. To verify the impact of the Euler bends in the coupling region, FDTD simulations were implemented. Additionally, we analyzed a constant-bend waveguide with a radius of $80 \mu\text{m}$ and a width of $0.8 \mu\text{m}$, as the length of the constant bend structure with this radius is equal to the Euler bend structure we used. After simulation, we could see that the coupling coefficient increased while the transmission coefficient decreased with the coupling gap decreasing when $w_1 = w_2 = 0.8 \mu\text{m}$, as shown in Figure 3a,b, respectively. Based on the evanescent-field coupling mechanism, as the coupling spacing between the waveguide and the microring increases, the overlap of the evanescent fields of the two decreases, which would consequently lead to a reduction in the coupling coefficient. However, if w_{gap} continues to decrease, the coupling gap would become so small and then hard to be manufactured even if the desired coupling coefficient of 0.15 could be reached. Thus, another method to increase the coupling coefficient κ^2 is to decrease the width of the incident waveguide w_1 .

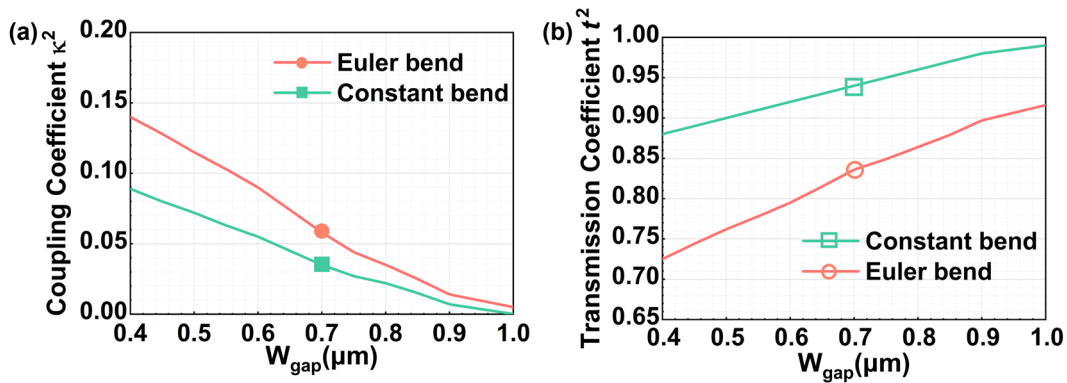


Figure 3. (a) The coupling coefficient κ^2 and (b) the transmission coefficient t^2 vary with w_{gap} in the coupling region at the wavelength of 1550 nm.

The coupling and the transmission coefficients with the variation in the width of the incident waveguide w_1 at the wavelength of 1550 nm are shown in Figures 4a and 4b, respectively, when the coupling gap is 0.7 μm . As the width of the bus waveguide narrowed, the confinement ability of the waveguide for light changed. In a narrower bus waveguide, the propagation mode of light was more inclined to spread around, enabling more optical fields to enter the coupling region with the ring cavity waveguide. According to the coupled-mode theory, the coupling coefficient is proportional to the overlap integral of the mode fields of the two coupled waveguides. The coupling coefficient, described as the light coupling strength between two waveguides, increases when the overlap of the optical field between the two waveguides increases [35]. Therefore, choosing a w_1 that is smaller than w_2 is a viable approach. The slow leakage of the optical field between the two waveguides for coupling can realize low-loss coupling. Meanwhile, the design can increase the coupling coefficient κ^2 and has relatively lower requirements for the precision of coupling spacing, which is more favorable for practical fabrication and provides higher expandability. It can be observed that when w_1 was smaller than w_2 , the coupling coefficient increased, and the coupling coefficient κ^2 was close to our desired value of 0.15 when $w_1 = 0.6 \mu\text{m}$. Therefore, the coupling gap $w_{\text{gap}} = 0.7 \mu\text{m}$ and an incident waveguide width $w_1 = 0.6 \mu\text{m}$ were adopted for the modified racetrack resonator.

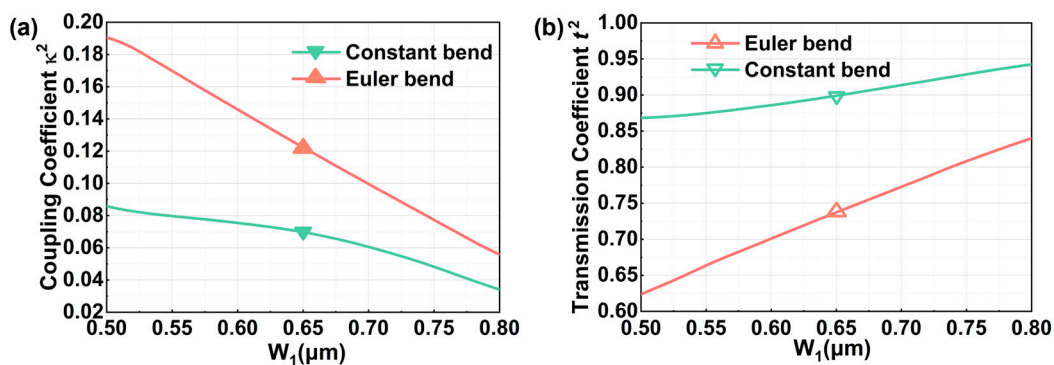


Figure 4. (a) The coupling coefficient κ^2 and (b) the transmission coefficient t^2 vary with w_1 in the coupling region at the wavelength of 1550 nm.

Below, the Q factor and BW with the variation of the straight waveguide length L_c are shown in Figure 5. It can be found that the straight waveguide length was calculated to be approximately 90 μm when the bandwidth was set to 30 GHz, as described above. But, considering that the tuning efficiency was directly proportional to the straight waveguide

length, the final length of the straight waveguide was designed to be 100 μm along with a bandwidth of approximately 29 GHz to increase the tuning efficiency.

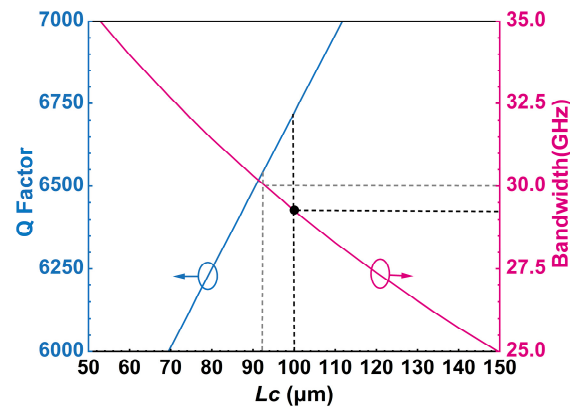


Figure 5. The BW and Q factor performances with the variation in L_c of the resonator.

The performance of the proposed EO-MRM with the optimized structure parameters were studied by a comparison of the conventional bend design. Figure 6a shows that the coupling and the transmission coefficients varied with the wavelength when the coupling gap was 0.7 μm and the incident waveguide width was 0.6 μm . As analyzed previously, the introduction of the Euler bend led to an increase in the coupling coefficient and a decrease in the transmission coefficient, subsequently resulting in an increase in bandwidth. As shown in Figure 6b, by introducing Euler bends in the coupling region, on the one hand, the extinction ratio significantly improved, with an increase of 35 dB. On the other hand, its 3 dB linewidth increased from 0.055 nm to 0.118 nm, and the increase in linewidth was quite beneficial for the enhancement of bandwidth. At the same time, it can be calculated that the circumference of the constant bend waveguide with a radius of 80 μm was approximately 503 μm . In contrast, the effective circumference of the Euler bend waveguide with a radius R_{min} of 30 μm and a radius R_{max} of 1500 μm was approximately 366 μm . This result indicates that the employed Euler bend could effectively reduce the footprint of the proposed device.

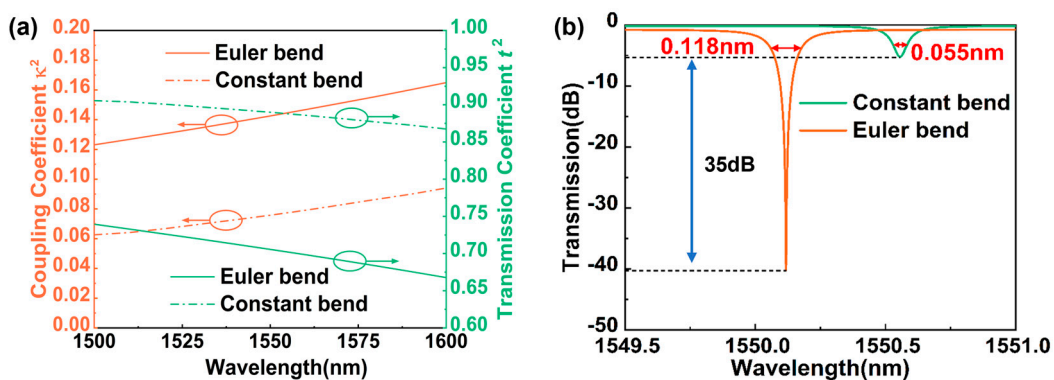


Figure 6. (a) The coupling and transmission coefficients with a variation in wavelength, when $w_{\text{gap}} = 0.7 \mu\text{m}$ and $w_1 = 0.6 \mu\text{m}$. (b) Transmission spectrum of the resonator with different bends used in the coupling region at the wavelength of 1550 nm.

3.2. Electrode Design and Optimization

After optimizing the desired high ER and BW, we performed further optimization to improve the tuning efficiency. To achieve a high tuning efficiency, a racetrack-shaped structure for the microring modulator was employed with the top view shown in Figure 7a,

in which the electrodes were loaded on both sides of the straight waveguides with a G-S-S-G electrode design. Moreover, the metal electrode was designed into a double-layer structure to improve the interaction of electric and light fields. This configuration allowed for the modulation effect on both sides of the waveguide to be combined, maximizing the utilization of the EO effect of LN.

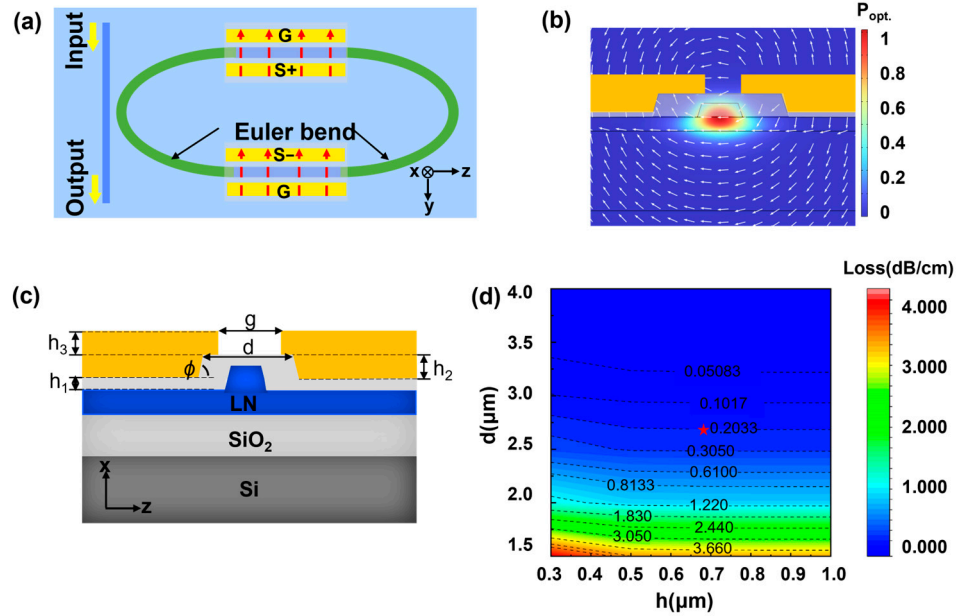


Figure 7. (a) A top view of the proposed tunable racetrack resonator with double-layer electrodes. (b) The simulated TE optical mode field profile at 1550 nm and the electric field between the double-layer electrodes. Here, the TFLN waveguide was formed by a 300 nm × 0.8 μm LN loading ridge. (c) A schematic of a unit cell of the electrode structure. (d) The simulation result of the influence of h and d on metal loss.

The tuning efficiency of the MRM is defined as follows:

$$\frac{\Delta\lambda_{res}}{V} = ff \times \frac{\lambda_{res}}{n_g} \times \Delta n_{eff}(\text{per volt}) \tag{4}$$

Here, $\Delta\lambda_{res}$ is the shift in resonance, n_g is the optical group index of the unperturbed optical mode, and ff represents the impact of the curvature of microring/electrodes and the filling extent of the electrodes. According to the reference [36], when the MRM adopts a racetrack-shaped structure, the filling factor becomes as follows:

$$ff = ff_{straight} \frac{l_{straight}}{l_{straight} + l_{circular}} + ff_{circular} \frac{l_{circular}}{l_{straight} + l_{circular}} \tag{5}$$

where l is the physical length of each segment. Because $ff_{straight} = 1$ and $ff_{circular} \leq 0.25$, the optimal configuration occurs with the electrode arrangement of Figure 6a with the limitation that the straight section is much longer than the circular section. Thus, when the electrode arrangement of the proposed modulator is a G-S-S-G structure, the filling factor ff can achieve its maximum value, which results in the highest potential tuning efficiency.

Moreover, the change in the effective refractive index Δn_{eff} can also be used to further improve the tuning efficiency, as shown in Equation (4). In general, Δn_{eff} can be expressed under the influence of an electric field as follows:

$$\Delta n_{eff} = -\frac{n_e^3 r_{33} V}{2} \Gamma \tag{6}$$

where Γ is the overlap between the optical field.

Double-layer metal electrodes that are very close can lead to excessive optical loss. In order to estimate the loss (in dB/cm) of the optical mode, we calculated the attenuation coefficient (damping factor) of the electric field (α_E in units of m^{-1}) in COMSOL and converted it to optical power attenuation (dB/cm) using the following equation [25]:

$$\alpha \left[\frac{dB}{cm} \right] = \alpha_E [m^{-1}] \times 2 \times 0.0434 \tag{7}$$

The simulated metal loss and Δn_{eff} with the variation in the electrode gap obtained by COMSOL are shown in Figure 8. It can be observed that the metal absorption loss increased rapidly as the metal spacing decreased, as shown in Figure 8a, and the metal electrode was directly placed on the waveguide, as shown in the inset. As shown in Figure 7c, we provisionally set the upper metal spacing g to $2 \mu m$ and changed the value of d and h ($h = h_1 + h_2$). Through the simulation, we found that the influence of metal thickness (h) on metal loss was less significant compared to the metal spacing (d) in Figure 7d. Considering the fabrication of metal electrodes, h was designed to be $0.7 \mu m$. Moreover, we found that as d increased, loss decreased but the effective refractive index dropped and may have been worse than the design without cladding. Conversely, a smaller d led to greater loss but a higher effective refractive index. To obtain a large tuning efficiency, there was a tradeoff that should be made between the effective refractive index and the loss. Finally, d was determined to be $2.8 \mu m$, and more refined optimization in the spacing of the upper metal was implemented, as shown in Figure 8b. According to the reference [25], the metal loss within the range of $1.1 \text{ dB/cm} \sim 2.2 \text{ dB/cm}$ would be the acceptable value. When the bottom and top metal spacing were set to be $2.8 \mu m$ and $1.4 \mu m$, respectively, the metal loss was around 1.58 dB/cm , and Δn_{eff} could increase to 3.132×10^{-5} . So, the final structural parameters of the proposed modulator are shown in Table 1.

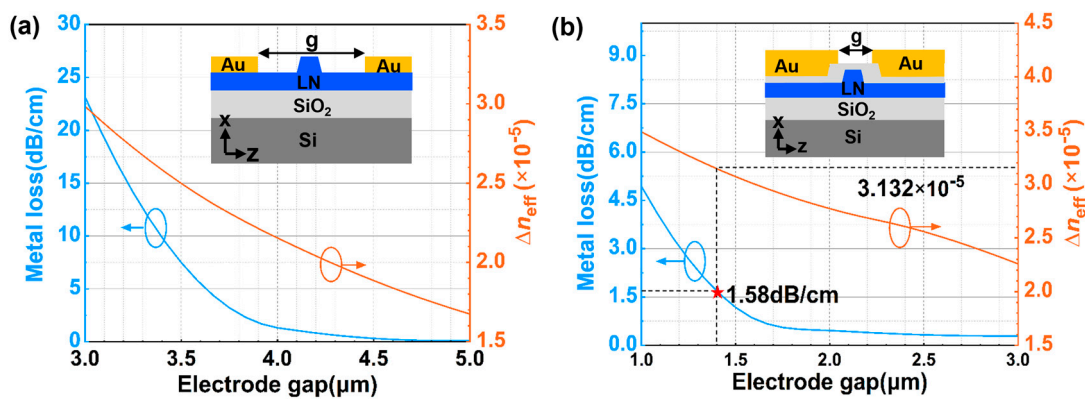


Figure 8. Metal loss analysis for different electrode designs. (a) Metal electrodes were placed directly on the waveguide. (b) A $2.8 \mu m$ -wide layer of SiO_2 was added between the double metal electrode and the waveguide.

Table 1. Design parameters of the proposed modulator.

w_1 (μm)	w_2 (μm)	w_{gap} (μm)	R_{min} (μm)	Electrode Gap (μm)	L_c (μm)
0.6	0.8	0.7	30	1.4	100

To test the performance of the proposed modulator considering the fabrication imperfections, the performance metrics were simulated when the geometric parameters varied in the ranges of typical fabrication imperfections (Table 2). In these simulations, for geometric

parameters whose fabrication imperfection mainly originated from alignment, we set a deviation of 20 nm. For each performance metric under the variation in a certain geometric parameter in a particular range, the worst value was depicted, with reference to [37]. As shown in Table 2, the extinction ratio, bandwidth, and tuning efficiency showed substantial robustness against fabrication imperfections. These results show that our modulator could maintain its functionality under typical fabrication imperfections.

Table 2. The performance of the proposed modulator with certain fabrication imperfections (the worst value).

Fabrication Imperfections	Metal Loss (dB/cm)	Extinction Ratio (dB)	Bandwidth (GHz)	Tuning Efficiency (pm/V)
None (ideal value)	1.58	38	29	8.24
ϕ varied from 70° to 75°	1.682	39.124	29.336	8.436
h_1 varied from 90 to 110 nm	1.503	37.630	28.727	8.113
h_2 varied from 290 to 310 nm	1.667	39.001	29.009	8.327
h_3 varied from 390 to 410 nm	1.575	37.777	28.872	8.227

4. Performance Analysis and Discussion

The final performances of the proposed MRM, including the transmission spectrum and Q factor, are shown in Figures 9a and 9b, respectively. It can be found that the free spectral range (FSR) was around 1.919 nm and the ER ranged from 30 dB to 51 dB. Then, the corresponding Q factor and ER of the MRM were approximately 6697 and 38 dB at 1550.118 nm; this can be deduced from Figure 9b,c. In all, it can be observed that the ER and Q factor were a good agreement with our design goal. The good tunability when the direct current (DC) bias voltage was applied is shown in Figure 9c. The change in voltage resulted in a shift in the resonant wavelength due to the change in the refractive index. When the voltage swept from 0 V to 25 V, the resonant wavelength shifted from 1550.118 nm to 1550.324 nm. Figure 9d shows the tuning efficiency of the proposed EO-MRM with the applied voltage after the data fitting, in which a linear tunability of 8.24 pm/V could be obtained. In a comparison with studies on the EO-MRMs based on LNOI or LN hybrid platforms, as shown in Table 3, the footprint of the proposed device is the smallest among the reported racetrack resonators and the proposed modulator performs better than other X-cut modulators in terms of the ER and BW. Overall, the comprehensive performance of the proposed device outperforms the X-cut EO-MRMs listed in the table.

Table 3. Performance comparison of different TFLN EO-MRMs.

Reference	Platform	Cut	Type	Tuning Efficiency (pm/V)	Extinction Ratio (dB)	Footprint (μm^2)	Bandwidth (GHz)
[11]	LNOI	X-cut	Racetrack	7/7.82 *	10	8.28×10^4	3.87 *
[12]	LNOI	Y-cut	Racetrack	0.32/0.61 *	>10	1.31×10^5	4/4.03 *
[23]	Si_3N_4 -LN	X-cut	Racetrack	2.9	30 *	1.32×10^6	2.98/2.61 *
[24]	Si_3N_4 -LN	X-cut	Ring	1.78/1.79 *	26.2/27 *	2.83×10^5	1.07/1.05 *
[25]	LNOI	Z-cut	Ring	9/8.9 *	20/22.5 *	3.60×10^3	28/35.61 *
[26]	LNOI	X-cut	Ring	10.8/13.88 *	11	2.54×10^4	17.5/9.52 *
This work	LNOI	X-cut	Racetrack	8.24 *	38 *	1.92×10^4 *	29 *

* is the simulation result.

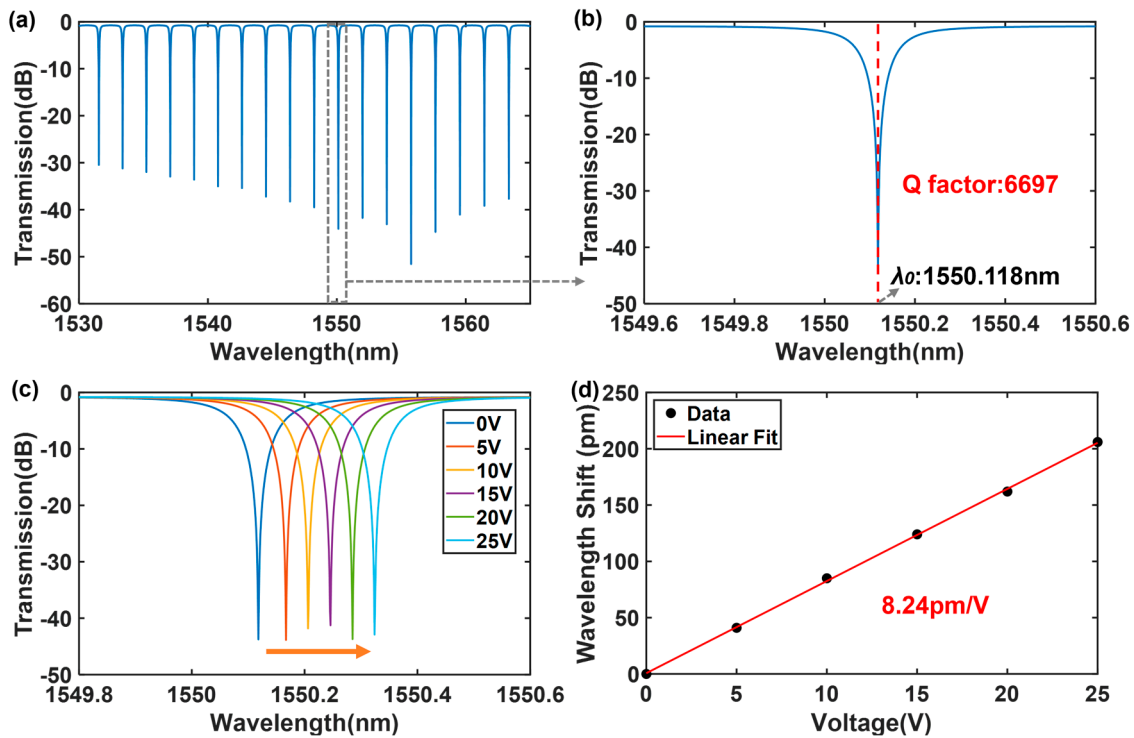


Figure 9. (a) The simulated transmission spectrum of the TE mode of the passive racetrack resonator. (b) The detailed spectrum at 1550.118 nm. (c) The spectrum under different voltages of the TE mode at 1550.118 nm. (d) Resonant wavelength shifts as a function of the applied voltage.

Based on existing fabrication techniques [38,39], the manufacturing process of the proposed EO modulator could be described as follows. First, the commercially available lithium niobate wafer with a thickness of 600 nm can be selected, and the waveguide structure is expected to be patterned through electron beam lithography (EBL). Then, the argon-based reactive ion etching (RIE) technique can be used to further etch the lithium-niobate to the desired thickness and sidewall angle. Subsequently, Plasma-Enhanced Chemical Vapor Deposition (PECVD) can be used to deposit the SiO₂ layer. It should be noted that if the SiO₂ layer does not meet the design requirements after PECVD, chemical mechanical polishing (CMP) will be needed. Next, the bottom electrode of a specific thickness is supposed to be patterned using a self-alignment lift-off process. In this process, a portion of the SiO₂ layer is expected to be etched away and filled with a metal layer using the same resisting layer for patterning. Finally, the top electrode is predicted to be fabricated using another round of the lift-off process. It can be seen from the above analysis that the proposed device can be fabricated based on current manufacturing techniques. However, due to the limitations of our current conditions, we did not fabricate and test the proposed device for the time being.

5. Conclusions

In summary, the design of a high-performance EO-MRM based on X-cut LNOI was proposed in this study. Specifically, we introduced modified Euler bend waveguides in the coupling region and a width-reduced input waveguide to increase the coupling coefficient and reduce the transmission coefficient and then to realize the high extinction ratio and broad bandwidth. Moreover, the double-layer G-S-S-G electrode structure in the straight waveguide section and SiO₂ cladding between LN and the metal electrode of the racetrack resonator were applied to further improve the tuning efficiency. After parameters optimization, the designed EO-MRM could achieve an *ER* of up to 38 dB and a BW of

29 GHz, along with a tunability of up to 8.24 pm/V, and the proposed device footprint was $1.92 \times 10^4 \mu\text{m}^2$. Our design paves the way for compact, high-performance electro-optic modulators, leading to potential applications in optical communications, microwave photonics, signal processing, and so on.

Author Contributions: Conceptualization and methodology, Z.C. and W.Z.; investigation, Z.C. and J.L.; data curation, Z.C. and H.L.; writing—original draft preparation, Z.C.; writing—review and editing, J.L., Q.H., Y.H. and Y.Q. All authors have read and agreed to the published version of the manuscript.

Funding: This work is partly supported by the National Key R&D Program of China (2023YFB2906304), the National Natural Science Foundation of China (U22A2087, 62022029, 62105381), the Guangdong Introducing Innovative and Entrepreneurial Teams of “The Pearl River Talent Recruitment Program” (2019ZT08X340), the Guangdong Guangxi Joint Science Key Foundation (2021GXNSFDA076001), and the Guangdong Basic and Applied Basic Research Foundation (2023A1515010877).

Institutional Review Board Statement: Not applicable.

Informed Consent Statement: Not applicable.

Data Availability Statement: Data underlying the results presented in this paper are not publicly available at this time but may be obtained from the authors upon reasonable request.

Acknowledgments: The authors acknowledge the research’s financial support from the National Natural Science Foundation of China, Guangdong Guangxi Joint Science Key Foundation, and Guangdong Basic and Applied Basic Research Foundation. The authors thank the Key Laboratory of Photonic technology for Integrated Sensing and Communication for simulation tools.

Conflicts of Interest: The authors declare no conflicts of interest.

References

1. Weis, R.S.; Gaylord, T.K. Lithium niobate: Summary of physical properties and crystal structure. *Appl. Phys. A* **1985**, *37*, 191–203. [[CrossRef](#)]
2. Saravi, S.; Pertsch, T.; Setzpfandt, F. Lithium Niobate on Insulator: An Emerging Platform for Integrated Quantum Photonics. *Adv. Opt. Mater.* **2021**, *9*, 2100789. [[CrossRef](#)]
3. Chen, G.; Gao, Y.; Lin, H.L.; Danner, A.J. Compact and Efficient Thin-Film Lithium Niobate Modulators. *Adv. Photonics Res.* **2023**, *4*, 2300229. [[CrossRef](#)]
4. Kong, Y.; Bo, F.; Wang, W.; Zheng, D.; Liu, H.; Zhang, G.; Rupp, R.; Xu, J. Recent Progress in Lithium Niobate: Optical Damage, Defect Simulation, and On-Chip Devices. *Adv. Mater.* **2020**, *32*, e1806452. [[CrossRef](#)] [[PubMed](#)]
5. Boes, A.; Corcoran, B.; Chang, L.; Bowers, J.; Mitchell, A. Status and Potential of Lithium Niobate on Insulator (LNOI) for Photonic Integrated Circuits. *Laser Photonics Rev.* **2018**, *12*, 1700256. [[CrossRef](#)]
6. Xue, Y.; Gan, R.; Chen, K.; Chen, G.; Ruan, Z.; Zhang, J.; Liu, J.; Dai, D.; Guo, C.; Liu, L. Breaking the bandwidth limit of a high-quality-factor ring modulator based on thin-film lithium niobate. *Optica* **2022**, *9*, 1131–1137. [[CrossRef](#)]
7. Feng, H.; Zhang, K.; Sun, W.; Ren, Y.; Zhang, Y.; Zhang, W.; Wang, C. Ultra-high-linearity integrated lithium niobate electro-optic modulators. *Photonics Res.* **2022**, *10*, 2366–2373. [[CrossRef](#)]
8. Ren, T.; Zhang, M.; Wang, C.; Shao, L.; Reimer, C.; Zhang, Y.; King, O.; Esman, R.; Cullen, T.; Loncar, M. An Integrated Low-Voltage Broadband Lithium Niobate Phase Modulator. *IEEE Photonics Technol. Lett.* **2019**, *31*, 889–892. [[CrossRef](#)]
9. Ying, P.; Tan, H.; Zhang, J.; He, M.; Xu, M.; Liu, X.; Ge, R.; Zhu, Y.; Liu, C.; Cai, X. Low-loss edge-coupling thin-film lithium niobate modulator with an efficient phase shifter. *Optics Lett.* **2021**, *46*, 1478–1481. [[CrossRef](#)] [[PubMed](#)]
10. Xu, M.; Zhu, Y.; Pittalà, F.; Tang, J.; He, M.; Ng, W.C.; Wang, J.; Ruan, Z.; Tang, X.; Kuschnerov, M.; et al. Dual-polarization thin-film lithium niobate in-phase quadrature modulators for terabit-per-second transmission. *Optica* **2022**, *9*, 61–62. [[CrossRef](#)]
11. Wang, C.; Zhang, M.; Stern, B.; Lipson, M.; Lončar, M. Nanophotonic lithium niobate electro-optic modulators. *Opt. Express* **2018**, *26*, 1547–1555. [[CrossRef](#)] [[PubMed](#)]
12. Mahmoud, M.; Cai, L.; Bottenfield, C.; Piazza, G. Lithium Niobate Electro-Optic Racetrack Modulator Etched in Y-Cut LNOI Platform. *IEEE Photonics J.* **2018**, *10*, 1–10. [[CrossRef](#)]
13. Li, M.; Ling, J.; He, Y.; Javid, U.A.; Xue, S.; Lin, Q. Lithium niobate photonic-crystal electro-optic modulator. *Nat. Commun.* **2020**, *11*, 4123. [[CrossRef](#)]

14. Wooten, E.; Kissa, K.; Yi-Yan, A.; Murphy, E.; Lafaw, D.; Hallemeier, P.; Maack, D.; Attanasio, D.; Fritz, D.; McBrien, G.; et al. A review of lithium niobate modulators for fiber-optic communications systems. *IEEE J. Sel. Top. Quantum Electron.* **2000**, *6*, 69–82. [[CrossRef](#)]
15. Xie, Z.; Bo, F.; Lin, J.; Hu, H.; Cai, X.; Tian, X.-H.; Fang, Z.; Chen, J.; Wang, M.; Chen, F.; et al. Recent development in integrated Lithium niobate photonics. *Adv. Phys.* **2024**, *9*, 2322739. [[CrossRef](#)]
16. Alam, M.S.; Li, X.; Jacques, M.; Xing, Z.; Samani, A.; El-Fiky, E.; Koh, P.C.; Plant, D.V. Net 220 Gbps/λ IM/DD Transmission in O-Band and C-Band With Silicon Photonic Traveling-Wave MZM. *J. Light. Technol.* **2021**, *39*, 4270–4278. [[CrossRef](#)]
17. Eppenberger, M.; Messner, A.; Bitachon, B.I.; Heni, W.; Blatter, T.; Habegger, P.; Destraz, M.; De Leo, E.; Meier, N.; Del Medico, N.; et al. Resonant plasmonic micro-racetrack modulators with high bandwidth and high temperature tolerance. *Nat. Photonics* **2023**, *17*, 360–367. [[CrossRef](#)]
18. Han, C.; Jin, M.; Tao, Y.; Shen, B.; Wang, X. Recent Progress in Silicon-Based Slow-Light Electro-Optic Modulators. *Micromachines* **2022**, *13*, 400. [[CrossRef](#)]
19. Han, C.; Zheng, Z.; Shu, H.; Jin, M.; Qin, J.; Chen, R.; Tao, Y.; Shen, B.; Bai, B.; Yang, F.; et al. Slow-light silicon modulator with 110-GHz bandwidth. *Sci. Adv.* **2023**, *9*, 5339. [[CrossRef](#)]
20. Li, M.; Wang, L.; Li, X.; Xiao, X.; Yu, S. Silicon intensity Mach Zehnder modulator for single lane 100 Gb/s applications. *Photonics Res.* **2018**, *6*, 109–116. [[CrossRef](#)]
21. Yu, F.; Zeng, Z.; Ji, X.; Tang, K.; Xin, Y.; Wu, G.; Mao, D.; Gu, T.; Huang, Q.; Jiang, W. Silicon electro-optic modulators based on microscopic photonic structures: From principles to advanced modulation formats. *J. Phys. D Appl. Phys.* **2023**, *56*, 443002. [[CrossRef](#)]
22. Mohammadi, M.; Soroosh, M.; Farmani, A.; Ajabi, S. Engineered FWHM enhancement in plasmonic nanoresonators for multiplexer/demultiplexer in visible and NIR range. *Optik* **2023**, *274*, 170583. [[CrossRef](#)]
23. Ahmed, A.N.R.; Shi, S.; Mercante, A.J.; Prather, D.W. High-performance racetrack resonator in silicon nitride—Thin film lithium niobate hybrid platform. *Opt. Express* **2019**, *27*, 30741–30751. [[CrossRef](#)] [[PubMed](#)]
24. Ahmed, A.N.R.; Shi, S.; Zablocki, M.; Yao, P.; Prather, D.W. Tunable hybrid silicon nitride and thin-film lithium niobate electro-optic microresonator. *Opt. Lett.* **2019**, *44*, 618–621. [[CrossRef](#)]
25. Bahadori, M.; Yang, Y.; Hassanien, A.E.; Goddard, L.L.; Gong, S. Ultra-efficient and fully isotropic monolithic microring modulators in a thin-film lithium niobate photonics platform. *Opt. Express* **2020**, *28*, 29644–29661. [[CrossRef](#)] [[PubMed](#)]
26. Lin, Q.; Hu, Y.; Li, Y.; Chen, H.; Liu, R.; Tian, G.; Qiu, W.; Yang, T.; Guan, H.; Lu, H. Versatile Tuning of Compact Microring Waveguide Resonator Based on Lithium Niobate Thin Films. *Photonics* **2023**, *10*, 424. [[CrossRef](#)]
27. Tan, Y.; Niu, S.; Billet, M.; Singh, N.; Niels, M.; Vanackere, T.; Van Kerrebrouck, J.; Roelkens, G.; Kuyken, B.; Van Thourhout, D. Micro-transfer Printed Thin Film Lithium Niobate (TFLN)-on-Silicon Ring Modulator. *ACS Photonics* **2024**, *11*, 1920–1927. [[CrossRef](#)]
28. Yu, H.; Ying, D.; Pantouvaki, M.; Van Campenhout, J.; Absil, P.; Hao, Y.; Yang, J.; Jiang, X. Trade-off between optical modulation amplitude and modulation bandwidth of silicon micro-ring modulators. *Opt. Express* **2014**, *22*, 15178–15189. [[CrossRef](#)]
29. Sun, D.; Zhang, Y.; Wang, D.; Song, W.; Liu, X.; Pang, J.; Geng, D.; Sang, Y.; Liu, H. Microstructure and domain engineering of lithium niobate crystal films for integrated photonic applications. *Light Sci. Appl.* **2020**, *9*, 197. [[CrossRef](#)]
30. Sheng, Z.; Yue, L.; Zhao, Y.; Jin, G.; Zhang, Q.; Fu, S.; Wang, X.; Wang, X.; Wang, X. A high figure of merit of phonon-polariton waveguide modes with hbn/SiO₂/graphene/hBN ribs waveguide in mid-infrared range. *Heliyon* **2024**, *10*, e26727. [[CrossRef](#)]
31. Dong, P.; Liao, S.; Feng, D.; Liang, H.; Zheng, D.; Shafiiha, R.; Kung, C.-C.; Qian, W.; Li, G.; Zheng, X.; et al. Low V_{pp}, ultralow-We added page number, please checkenergy, compact, high-speed silicon electro-optic modulator. *Opt. Express* **2009**, *17*, 22484–22490. [[CrossRef](#)] [[PubMed](#)]
32. Mobini, E.; Espinosa, D.H.G.; Vyas, K.; Dolgaleva, K. AlGaAs Nonlinear Integrated Photonics. *Micromachines* **2022**, *13*, 991. [[CrossRef](#)]
33. Wei, C.; Li, J.; Jia, Q.; Li, D.; Liu, J. Ultrahigh-Q lithium niobate microring resonator with multimode waveguide. *Opt. Lett.* **2023**, *48*, 2465–2467. [[CrossRef](#)]
34. Zhang, L.; Jie, L.; Zhang, M.; Wang, Y.; Xie, Y.; Shi, Y.; Dai, D. Ultrahigh-Q silicon racetrack resonators. *Photonics Res.* **2020**, *8*, 684–689. [[CrossRef](#)]
35. Son, S.J.; Kim, S.; Yu, N.E.; Ko, D.K. Bus-waveguide-width Dependence of Evanescent Wave Coupling in a Microring Resonator. *Curr. Opt. Photon.* **2021**, *5*, 538–543.
36. Bahadori, M.; Goddard, L.L.; Gong, S. Fundamental electro-optic limitations of thin-film lithium niobate microring modulators. *Opt. Express* **2020**, *28*, 13731–13749. [[CrossRef](#)]
37. Qi, Y.; Zhang, Z.; Jia, W.; Chen, S.; Yang, Y.; Li, Y. Design of Ultracompact High-Speed-Integrated Lithium–Niobate PeriodicDielectric Waveguide Modulator. *Adv. Photonics Res.* **2022**, *3*, 2200050. [[CrossRef](#)]

38. Wu, R.; Gao, L.; Liang, Y.; Zheng, Y.; Zhou, J.; Qi, H.; Yin, D.; Wang, M.; Fang, Z.; Cheng, Y. High-Production-Rate Fabrication of Low-Loss Lithium Niobate Electro-Optic Modulators Using Photolithography Assisted Chemo-Mechanical Etching (PLACE). *Micromachines* **2022**, *13*, 378. [[CrossRef](#)] [[PubMed](#)]
39. Zhang, M.; Wang, C.; Kharel, P.; Zhu, D.; Lončar, M. Integrated lithium niobate electro-optic modulators: When performance meets scalability. *Optica* **2021**, *8*, 652–667. [[CrossRef](#)]

Disclaimer/Publisher’s Note: The statements, opinions and data contained in all publications are solely those of the individual author(s) and contributor(s) and not of MDPI and/or the editor(s). MDPI and/or the editor(s) disclaim responsibility for any injury to people or property resulting from any ideas, methods, instructions or products referred to in the content.